J. Fluid Mech. (2025), *vol*. 1002, A8, doi:10.1017/jfm.2024.1137

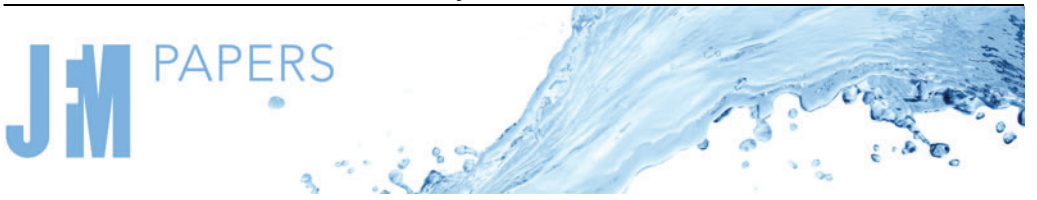

Droplet impact on a flexible disk

Xinping Zhou[1,2], **Yongqi Xu**[1], **Qi Zhang**[1], **Wanqiu Zhang**[1] and **Ze-Rui Peng**[3,4,†]

[1]School of Mechanical Science and Engineering, Huazhong University of Science and Technology, Wuhan 430074, PR China

[2]State Key Laboratory of Intelligent Manufacturing Equipment and Technology, Huazhong University of Science and Technology, Wuhan 430074, PR China

[3]Department of Mechanics, School of Aerospace Engineering, Huazhong University of Science and Technology, Wuhan 430074, PR China

[4]Hubei Key Laboratory for Engineering Structural Analysis and Safety Assessment, Wuhan 430074, PR China

(Received 15 November 2023; revised 6 October 2024; accepted 23 November 2024)

In this paper, we simulate the process of two-dimensional axisymmetric fluid–structure coupling of a droplet impacting on a flexible disk. The effects of dimensionless disk stiffness ($K = 0.1$–1000), Weber number ($We = 1$–500) and contact angle ($\theta = 130°$ and $60°$) on the dynamics of the droplet impacting on the flexible disk are analysed. The results indicate that there are five typical impact modes for a hydrophobic surface ($\theta = 130°$) and four typical impact modes for a hydrophilic surface ($\theta = 60°$) within the range of considered parameters. The analysis of spreading factor reveals that a part of the energy is transferred to the substrate, which is manifested as a weakening of the droplet spreading, when the substrate deforms downwards due to the droplet impact; the squeezing of the droplet causes a tendency to flow from the centre of the droplet to the edge, which is manifested as an enhancement of the droplet spreading, when the substrate recovers from the downward deformation. The effect of the substrate flexibility on the maximum spreading factor depends on the competition of the two mechanisms above. Based on this, a modified scaling law of β_{max} has been proposed by introducing the effective Weber number (We_m). The analysis of impact force demonstrates that the peak of the impact force is related to the deflection of the flexible substrate which is different from that of a rigid wall; and three typical processes of impact force variation have been summarised. In addition, unlike the rigid substrate scenario, there is an energy interaction between the droplet and the flexible substrate after impact occurs, which is classified as three typical energy transformation processes.

Key words: capillary flows, flow–structure interactions, drops

† Email addresses for correspondence: zeruipeng@hust.edu.cn

1. Introduction

The impact of droplets on solid surfaces is a common phenomenon in both nature and engineering, seen in processes such as inkjet printing (Derby 2010; Lohse 2022), raindrop impact (Abuku *et al.* 2009; Gart *et al.* 2015; Gilet & Bourouiba 2015; Kim *et al.* 2020), droplet freezing (Mishchenko *et al.* 2010; Jung *et al.* 2012) and pesticide deposition (Wirth, Storp & Jacobsen 1991; Bergeron *et al.* 2000). After impact, droplet dynamics can be divided into two stages: spreading and recoiling. In the spreading stage, the kinetic energy is converted into surface energy and dissipated through viscosity, until the droplet reaches its maximum spread. During the recoiling stage, surface tension drives the droplet to retract, converting the surface energy back into kinetic energy, with some energy lost through viscous dissipation. Droplets impacting on a dry rigid substrate can exhibit different modes, including deposition, prompt splashing, corona splashing, receding break-up, partial rebound or complete rebound (Rioboo, Tropea & Marengo 2001). The outcome depends on the physical parameters, such as droplet viscosity, impact velocity, surface tension coefficient, solid surface roughness and surface wettability (Josserand & Thoroddsen 2016).

Previous research is mainly focused on dynamics of a droplet impacting on rigid surfaces. However, many real-world surfaces, such as leaves, umbrellas, clothing fabrics, are flexible. The effects of substrate flexibility on droplet impact dynamics are still less understood, though the limited studies provide insights. For example, Weisensee *et al.* (2016) observed that flexible substrates can rebound, returning kinetic energy to the droplet and reducing the contact time by up to 50 %, a phenomenon termed the 'springboard effect'. Huang *et al.* (2018) found that flexible, superhydrophobic cotton significantly reduces the retraction time and overall contact duration once the impact velocity exceeds a threshold, due to energy stored in the substrate during droplet spreading. Other studies (e.g. Mangili *et al.* 2012; Chen *et al.* 2016; Vasileiou *et al.* 2016; Vasileiou, Schutzius & Poulikakos 2017), mostly using experimental methods, explored similar energy storage and release mechanisms, with flexible substrates enhancing droplet rebound and modifying the conditions required for various impact behaviours.

The role of flexibility in reducing splashing has also been investigated. Pepper, Courbin & Stone (2008) and Howland *et al.* (2016) observed that flexible substrates suppress droplet splashing, likely due to the early substrate deformation absorbing energy. Their experiments showed that splashing on the softest substrate requires approximately 70 % more kinetic energy than on a rigid surface. Further, Pegg, Purvis & Korobkin (2018) conducted analytical and numerical studies on the splashing dynamics when a droplet impacts a small flexible plate. They found that the oscillation of the flexible substrate can amplify the splash jet, a phenomenon not observed on rigid surfaces. Similarly, Dressaire *et al.* (2016) investigated droplet impact on a thin flexible fibre and found that the fibre's flexibility affects the threshold capture velocity in a nonlinear way.

Although experimental studies provide valuable insights, numerical simulations offer a more detailed and comprehensive analysis of droplet impact dynamics. However, most existing research on droplet impacts on flexible substrates is experimental, with very few numerical studies available. Xiong, Huang & Lu (2020) conducted two-dimensional (2-D) numerical simulations of droplet impacts on a flexible substrate simply supported at both ends, investigating the effects of Weber numbers within a limited range on droplet impact dynamics. However, these 2-D simulations showed significant discrepancies when compared with actual droplet impact behaviour. In a more recent study, Ma & Huang (2023) simulated droplet impacts on both 2-D and three-dimensional flexible rectangular substrates, also simply supported at both ends. Their research focused on the influence

of Weber number, substrate bending stiffness and solid-to-liquid density ratio on the maximum spreading factor, proposing a scaling law for it. However, they did not analyse other dynamic characteristics influenced by substrate flexibility, such as impact forces. Currently, the dynamic behaviour of droplets impacting a flexible substrate remains unclear, and the underlying mechanisms governing droplet–flexible substrate interactions are still not well understood.

In this study, we numerically simulate a droplet impacting a simply supported flexible circular disk, differing from the rectangular substrates examined by Xiong *et al.* (2020) and Ma & Huang (2023). The simulations are conducted within a 2-D axisymmetric framework across a wide range of Weber numbers ($We = 1$–500). We focus on the effects of the Weber number and substrate bending stiffness on droplet impact dynamics, providing a comprehensive analysis of droplet–flexible substrate interactions. This includes impact modes, maximum spreading factor (β_{max}), spreading time, scaling laws for β_{max}, impact forces, energy conversion and more. While the primary analysis focuses on hydrophobic surfaces (contact angle $\theta = 130°$), we also investigate the behaviour of droplets impacting a hydrophilic flexible substrate ($\theta = 60°$) towards the end of this paper.

The remainder of this paper is organised as follows: § 2 describes the computational model, including the physical problem, mathematical formulation, numerical methods and numerical validations. Section 3 presents results and discussions on the dynamics of droplets impacting on a flexible disk. Finally, concluding remarks are provided in § 4.

2. Computational model

2.1. *Physical model and mathematical formulation*

The schematic of a droplet impacting on a flexible circular plate is shown in figure 1. At the initial moment, a spherical droplet with a diameter D_0, density ρ_l and viscosity μ_l has a downward impact velocity U_0; directly below the droplet at a distance H ($= 0.5D_0$), a flat flexible disk with thickness h, diameter L, density ρ_s and Young's modulus E is simply supported at its edge. The droplet is surrounded by a gas with density ρ_g and viscosity μ_g. In numerical simulations, the gravity is not considered. After impacting, the droplet spreads on the deformed substrate. In this process, the droplet impact gives rise to the deformation and the motion of the substrate, which, in turn, affects the droplet dynamics. As shown in figure 1(*b*), the spreading factor (β) is defined. At the centre of the substrate, the droplet's thickness and the substrate's deflection are denoted by y and d, respectively. A 2-D axisymmetric model is adopted and the gravity is neglected. The letters r and z represent the radial and axial coordinates, respectively, and the substrate is initially located at $z = 0$.

In this system, the fluid flow is governed by the incompressible Navier–Stokes equations,

$$\rho_f \frac{\partial \boldsymbol{v}_f}{\partial t} + \rho_f(\boldsymbol{v}_f \cdot \boldsymbol{\nabla})\boldsymbol{v}_f = \boldsymbol{\nabla} \cdot [-p\boldsymbol{I} + \mu(\boldsymbol{\nabla}\boldsymbol{v}_f + (\boldsymbol{\nabla}\boldsymbol{v}_f)^{\mathrm{T}})] + \boldsymbol{F}_{st} + \rho_f \boldsymbol{g}, \tag{2.1}$$

$$\boldsymbol{\nabla} \cdot \boldsymbol{v}_f = 0, \tag{2.2}$$

where ρ_f is the fluid density, $\boldsymbol{v}_f$ is the fluid velocity vector, $\boldsymbol{I}$ is the unit tensor, μ_f is the fluid dynamic viscosity, p is the pressure, $\boldsymbol{F}_{st}$ is the surface tension force term of the fluid and t is the time. The flexible substrate is modelled as a shell, the thickness of which is negligible. The deformation and motion of the shell are described by the following

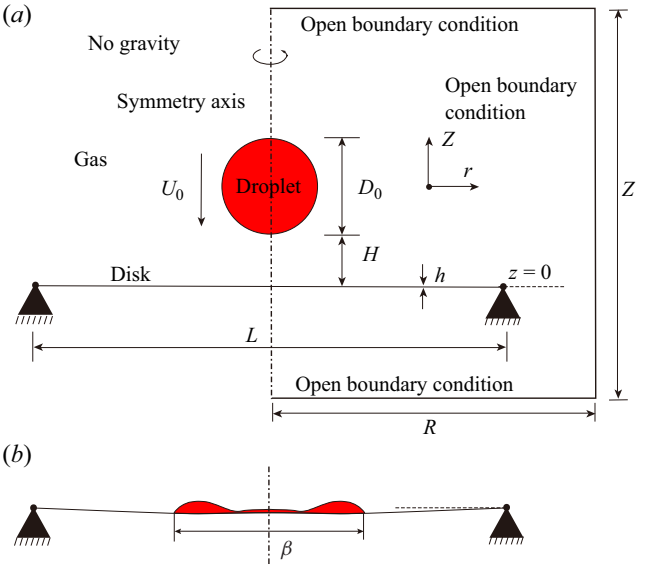

Figure 1. Schematic of a droplet impacting on a flexible circular disk: (*a*) initial configuration; (*b*) an instant of the droplet spreading on the deformed substrate.

structural equations:

$$\rho_s \frac{\partial^2 \boldsymbol{u}_s}{\partial t^2} = \nabla \cdot (\boldsymbol{FS})^{\mathrm{T}} + \rho_s \boldsymbol{g}, \tag{2.3}$$

where ρ_s is the structure density and $\boldsymbol{u}_s$ is the displacement vector. In our study, gravity is neglected, i.e. $\boldsymbol{g} = \boldsymbol{0}$. The deformation gradient tensor $\boldsymbol{F}$ and the second Piola–Kirchhoff stress tensor $\boldsymbol{S}$ are defined as

$$\boldsymbol{F} = \boldsymbol{I} + \nabla \boldsymbol{u}_s, \tag{2.4}$$

$$\boldsymbol{S} = J\boldsymbol{F}^{-1}\boldsymbol{\sigma}_s\boldsymbol{F}^{-T}, \tag{2.5}$$

respectively, where $\boldsymbol{\sigma}_s$ is the Cauchy stress tensor and the volume factor J is given by

$$J = \det(\boldsymbol{F}) = \frac{\mathrm{d}V}{\mathrm{d}V_0}, \tag{2.6}$$

where V_0 is the volume before deformation and V is the volume after deformation. The strain tensor corresponding to the second type of Piola–Kirchhoff stress tensor is the Green–Lagrangian strain tensor:

$$\boldsymbol{E} = \tfrac{1}{2}(\boldsymbol{F}^T\boldsymbol{F} - \boldsymbol{I}). \tag{2.7}$$

The flexible disk in this problem is an isotropic linear elastic material, then $\boldsymbol{S}$ and $\boldsymbol{E}$ satisfy Hooke's law:

$$\boldsymbol{S} = \lambda(\mathrm{tr}\,\boldsymbol{E})\boldsymbol{I} + 2G\boldsymbol{E}, \tag{2.8}$$

where λ and G are the Lamé coefficient and shear modulus, respectively, which can be calculated from the Young's modulus E and Poisson's ratio v of the material:

$$\lambda = \frac{vE}{(1+v)(1-2v)}, \tag{2.9}$$

$$G = \frac{E}{2(1+v)}. \tag{2.10}$$

For the fluid–structure interaction (FSI) boundary, the conditions of velocity compatibility and stress balance must be satisfied:

$$\frac{\partial \boldsymbol{u}_s}{\partial t} = \boldsymbol{v}_f, \tag{2.11}$$

$$\boldsymbol{n} \cdot \boldsymbol{\sigma}_s = \boldsymbol{n} \cdot \boldsymbol{\sigma}_f, \tag{2.12}$$

where the unit vector $\boldsymbol{n}$ is normal to the solid boundary, and fluid stress $\boldsymbol{\sigma}_f$ is given by

$$\boldsymbol{\sigma}_f = -p\boldsymbol{I} + \mu_f[\nabla \boldsymbol{v}_f + (\nabla \boldsymbol{v}_f)^{\mathrm{T}}]. \tag{2.13}$$

In the present study, we choose ρ_l, D_0 and σ as characteristic quantities. The corresponding reference speed $U_{ref} = \sqrt{\sigma/(\rho_l D_0)}$. Thus, the following dimensionless governing parameters are given: the Weber number $We = \rho_l U_0^2 D_0/\sigma$, the Reynolds number $Re = \rho_l U_0 D_0/\mu_l$, the liquid-to-gas density ratio $\rho_r = \rho_l/\rho_g$, the liquid-to-gas viscosity ratio $\mu_r = \mu_l/\mu_g$, the bending stiffness $K = Eh^3/(\rho_l U_{ref}^2 L^3)$, the thickness of the flexible disk $h^* = h/D_0$, the disk diameter $L^* = L/D_0$ and the substrate-to-liquid density ratio $d_r = \rho_s/\rho_l$. The subscripts s, l and g denote the solid, the liquid and the gas, respectively. The dimensionless time $t^* = tU_{ref}/D_0$.

2.2. *Numerical method*

The numerical simulations are performed using software COMSOL Multiphysics (COMSOL 5.6), which provides a comprehensive platform for simulating FSI phenomena using the finite element method (FEM). In COMSOL Multiphysics, the governing equations for fluid and shell dynamics, i.e. (2.1)–(2.3) are converted into their weak form. The weak form equations are then discretised using FEM, with special attention given to mesh deformation to accurately capture the evolving interface between fluid and structure. The mesh for shell and fluid domains in COMSOL are provided in Appendix A. The fluid region is divided by the triangular elements. In the present model, the thickness of the shell is negligible. The variables of the shell, e.g. displacement vector, are defined on the midplane ($z = 0$). The shell elements are located on the midplane of the shell. In the simulation, the dynamic mesh deformation is required to account for changes in the geometry of both fluid and shell domains. We can specify mesh refinement criteria and employ adaptive meshing techniques to maintain computational accuracy while capturing complex fluid–structure interactions. Time discretisation is performed using the built-in backward differentiation formula in COMSOL. All variables are fully coupled using the constant Newton method (Deuflhard 1974), with a constant damping factor of 0.75. The Yeoh smoothing method (Yeoh 1993) is employed to constrain the mesh displacement, allowing for the maximum displacement before the mesh is inverted. The MUMPS solver is used for solving the linear systems of the coupled equations during the problem initialisation and transient process. For details regarding finite element discretisation,

meshing techniques and other technical aspects, please refer to the COMSOL User's Guide.

In the present simulations, the phase-field method is used to track the gas–liquid interface. In the phase-field method, the surface tension force is calculated based on the following expression:

$$\boldsymbol{F}_{st} = G\nabla\phi, \tag{2.14}$$

$$G = \lambda\left[-\nabla^2\phi + \frac{\phi(\phi^2-1)}{\varepsilon^2}\right] = \frac{\lambda}{\varepsilon^2}\psi, \tag{2.15}$$

where G is the chemical potential, γ is the mobility, λ is the mixing energy density, ε is the interface thickness parameter and ψ is the phase-field auxiliary variable. The diffusion interface is defined by a dimensionless phase-field variable ϕ, ranging from –1 to 1. Here, $\phi = -1$ and $\phi = 1$ correspond to the gas and liquid, respectively, with densities of ρ_g and ρ_l. To track the diffusion interface of two-phase fluids, the following phase-field equation (Cahn–Hilliard equation) is used:

$$\frac{\partial\phi}{\partial t} + \boldsymbol{v}_f \cdot \nabla\phi = \nabla \cdot \frac{\gamma\lambda}{\varepsilon^2}\nabla\psi, \tag{2.16}$$

$$\psi = -\nabla \cdot \varepsilon^2\nabla\phi + (\phi^2-1)\phi. \tag{2.17}$$

Here, σ, λ and ε have the following relationship:

$$\sigma = \frac{2\sqrt{2}\lambda}{3\varepsilon}. \tag{2.18}$$

In our simulation, we set the interface thickness ε to 0.75 h_m, where h_m represents the maximum grid size in the region through which the droplet passes. Additionally, γ determines the time scale of diffusion and is closely related to the interface thickness, i.e.

$$\gamma = \chi\varepsilon^2, \tag{2.19}$$

whereas χ represents the parameter for adjusting the mobility, which needs to be chosen precisely. If the value is too large, it excessively suppresses the convection term, and if it is too small, it becomes difficult to maintain the correct interface thickness. In our simulation, the value of the mobility adjustment parameter is determined by the following function:

$$\chi = \frac{8V_{max}}{9\sqrt{2}\sigma}, \tag{2.20}$$

where V_{max} is the maximum velocity in the entire computational domain at the current moment.

The phase-field method treats two-phase flow as a single-phase flow, where the properties in the flow domain such as density ρ and viscosity μ vary based on the volume fractions of different fluid phases,

$$\rho = \rho_g + (\rho_l - \rho_g)V_l, \tag{2.21}$$

$$\mu = \mu_g + (\mu_l - \mu_g)V_l. \tag{2.22}$$

The volume fractions of the light and heavy fluid phases are related through the phase-field variable ϕ, i.e.

$$V_g = \frac{1-\phi}{2}, \quad V_l = \frac{1+\phi}{2}. \tag{2.23a,b}$$

Open boundary conditions are applied to the upper, lower and lateral sides of the computational domain, while a wetted wall boundary condition is imposed on the substrate, which sets the mass flow rate passing through the wall to zero and specifies the contact angle of the liquid on the wall. This is described by the following equations:

$$\boldsymbol{n} \cdot \varepsilon^2 \nabla\phi = \varepsilon^2 \cos^{-1}\theta |\nabla\phi|, \tag{2.24}$$

$$\boldsymbol{n} \cdot \frac{\sigma\lambda}{\varepsilon^2}\nabla\psi = 0, \tag{2.25}$$

where θ is the static contact angle of the droplet on the disk substrate.

2.3. *Numerical validation*

Numerical simulations for the typical cases are carried out to quantitatively validate the reliability of the numerical method adopted in the present study. First, we have conducted the simulations for various contact angles within a realistic hysteresis range (i.e. $100° \pm 5°$) which is consistent with the experiments of Sikalo *et al.* (2002). According to the experiments of Sikalo *et al.* (2002), the key parameters in the simulations are set as follows: initial velocity $U_0 = 1.54$ m s^{-1}, surface tension coefficient $\sigma = 0.073$ N m^{-1}, viscosity $\mu_l = 1$ mPa · s, density $\rho_l = 996$ kg m^{-3}, diameter $D_0 = 2.7$ mm. The numerical simulations using the static contact angle model are conducted. According to the experiments of Sikalo *et al.* (2002), three static contact angles (SCA), i.e. 95°, 100° and 105°, are set. In addition, we conducted the numerical simulations using the quasi-dynamic contact angle model, in which the advancing and receding contact angles are 105° and 95°, respectively. Figures 2(*a*) and 2(*b*) show the variations of the dimensionless spreading diameter and apex height as a function of dimensionless time, respectively. As shown in figure 2, it can be observed that within the contact angle hysteresis range considered (i.e. $100° \pm 5°$), the experimental results and the numerical results using the static and quasi-dynamic contact angle models are generally in good agreement. Also, we can see from the numerical results that the discrepancies in the spreading factor and substrate deflection caused by using different contact angle models is not significant. In the present study, we use a static contact angle model for simulations, which is acceptable for some realistic situations where the contact angle hysteresis effect is not significant (Sikalo *et al.* 2002).

To validate the reliability of FSI calculations involving flexible structures, we conduct numerical simulations of the flow around a rigid cylinder with a flexible strip immersed in a uniform viscous flow. The results are provided in Appendix B. Further, we compared the present results with those of Ma & Huang (2023). In the simulations of Ma & Huang (2023), a liquid column impacting on the simply supported flexible plate has been considered; and the key dimensionless parameters are set as follows: the bending stiffness $K_B = EI/(\rho_l U_{ref}^2 L^3) = 0.01, 0.05$, the stretching stiffness $K_S = Eh/(\rho_l U_{ref}^2 L) = 100$, the Ohnesorge number $Oh = \mu/\sqrt{\rho_l D_0 \sigma} = 0.01$, the liquid-to-gas density ratio $\rho_r = 1000$, the liquid-to-gas viscosity ratio $\mu_r = 50$, the substrate span length $L/D_0 = 20$, the mass ratio $M_r = \rho_s h/\rho_l L = 0.01$ and the contact angle $\theta = 170°$. Figure 3 shows the maximum spreading factor β_{max} as a function of *We*. It is seen that for both rigid and flexible substrate cases, the present results and the results of Ma & Huang (2023) are generally

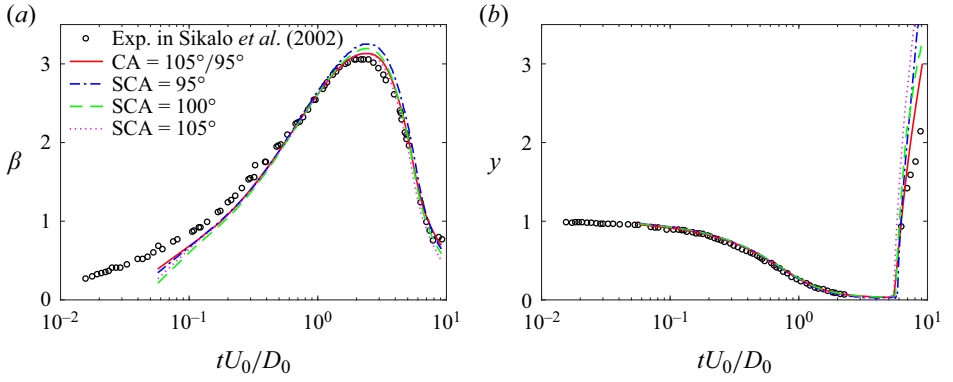

Figure 2. Time variations of (a) the spreading factor β and (b) the apex height y of the droplet impacting on a rigid wall. The results are obtained from experiments (Sikalo *et al.* 2002) and the present simulations using static and quasi-dynamic contact angle models. Three static contact angles (SCA) are set in the static contact angle model, i.e. SCA = 95°, 100° and 105°. In the quasi-dynamic contact angle model, the advancing and receding contact angles are 105° and 95°, respectively, which is denoted as 'CA= 105°/95°' in panel (a). The other key parameters in the simulations are set according to the experiments (Sikalo *et al.* 2002) as follows: initial velocity $U_0 = 1.54\ \mathrm{m\ s^{-1}}$, surface tension coefficient $\sigma = 0.073\ \mathrm{N\ m^{-1}}$, viscosity $\mu_l = 1\ \mathrm{mPa \cdot s}$, density $\rho_l = 996\ \mathrm{kg\ m^{-3}}$ and diameter $D_0 = 2.7\ \mathrm{mm}$.

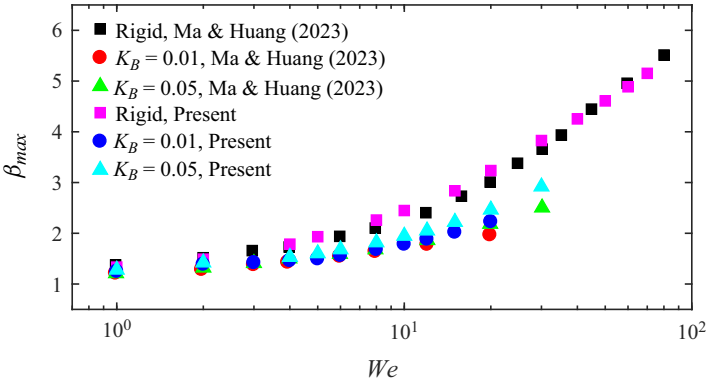

Figure 3. Maximum spreading factor β_{max} as a function of We in the present and Ma & Huang's (2023) simulations.

in good agreement. This illustrates the reliability of our numerical method in solving this multiphase FSI problem. It is noted that the 2-D axisymmetric model with the hydrophobic surfaces ($\theta = 130°$) are considered in the present simulations, which is different from the study of Ma & Huang (2023) and may cause the data discrepancies.

The grid independence analysis is performed. Figure 4(a,b) shows the time-dependent d and β calculated under three sets of mesh sizes, i.e. $\Delta x = 3D_0/200$, 1.5 $D_0/200$ and $D_0/200$. Here, the mesh size Δx denotes the maximum mesh size within the refined region at the initial moment. Correspondingly, the numbers of elements in the refined region are 64 560, 224 158 and 480 072, respectively. Since the unrefined domain is composed of air, variations in mesh size in this domain have negligible effects on the droplet–substrate coupling, and thus we limit the maximum size of the rough domain to $0.15D_0$ in mesh independence analysis. It is confirmed that $\Delta x/D_0 = 1.5/200$ is sufficient to achieve accurate results in the present simulations. Based on our convergence studies with different

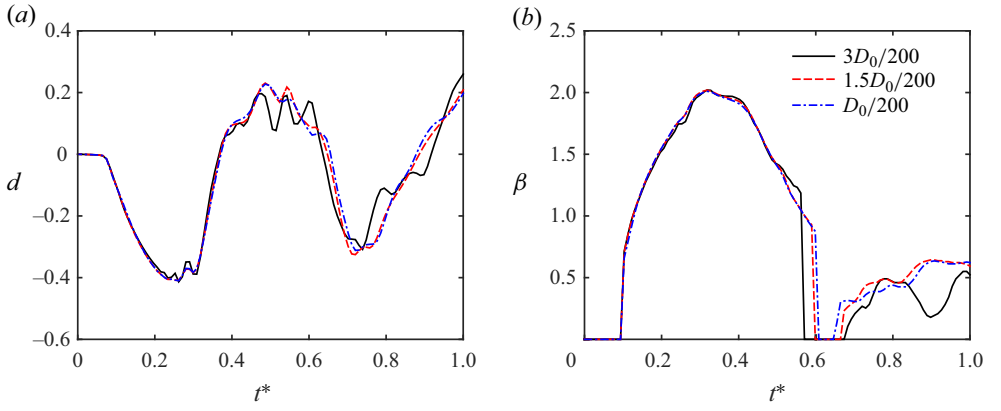

Figure 4. Grid independence test for $We = 50$, $K = 0.01$, $d_r = 1.25$, $h^* = 0.03$, $L^* = 6$, $\rho_r = 1000$, $\mu_r = 100$, $v = 0.45$ and $\theta = 130°$. (*a*) Substrate centre deflection and (*b*) spreading factor.

computational domains, the computational domain $R \times Z$ is chosen as $3.5D_0 \times 6.5D_0$. The domain is large enough so that the blocking effects of the boundaries are not significant.

3. Results and discussion

Here, we present some typical results of a droplet impacting on a flexible substrate. In our study, we focus on the effects of We and K on the droplet impact dynamics, while keeping other parameters constant unless otherwise specified. Specifically, $We \in [1, 500]$, $K \in [0.01, 1000]$, $Re = 1000$, $d_r = 1.25$, $h^* = 0.03$, $L^* = 6$, $\rho_r = 1000$, $\mu_r = 100$, $v = 0.45$ and $\theta = 130°$. Since the deformation of the substrate can be ignored during impact, the flexible substrate with $K = 1000$ is regarded as the rigid wall in the following sections.

3.1. *Impact mode and regime map*

In this section, we present the dynamics of a droplet impacting on a flexible substrate. It is found that compared with the rigid case, the droplet impacting on the flexible substrate has more complex dynamics due to the fluid–structure interaction. Based on a variety of simulations for a wide range of parameters considered here, we have identified five typical modes in terms of the droplet shape evolution during the impact, i.e. the ring-shaped rebound (RSR), the disc-shaped rebound (DSR), the jet-breakup rebound (JBR), the splashing rebound (SR) and edge-breakup rebound (EBR). It is worth noting that since the hydrophobic surface is considered in this section, the droplet bounces completely off the wall in all modes; according to whether the droplets are separated or broken during the rebound process, we can summarise the impact modes into two categories, namely, the intact rebound (IR, e.g. RSR and DSR) and breakup rebound (BR, e.g. JBR, SR or EBR). Note that the splashing phenomenon is considered as a special case of the droplet separation.

Figure 5 shows snapshots of a drop impacting on the flexible substrate for the cases of the typical modes. As shown in figure 5(*a*), for the case where $We = 10$ and $K = 1000$, corresponding to the RSR mode, the droplet spreading factor continues to increase in the spreading stage, while the apex height continues to decrease, the central part of the droplet gradually thins to form a liquid film or even breaks, and a liquid ring is formed when $t^* = 0.56$. Under the action of surface tension, the liquid ring retracts towards the centre.

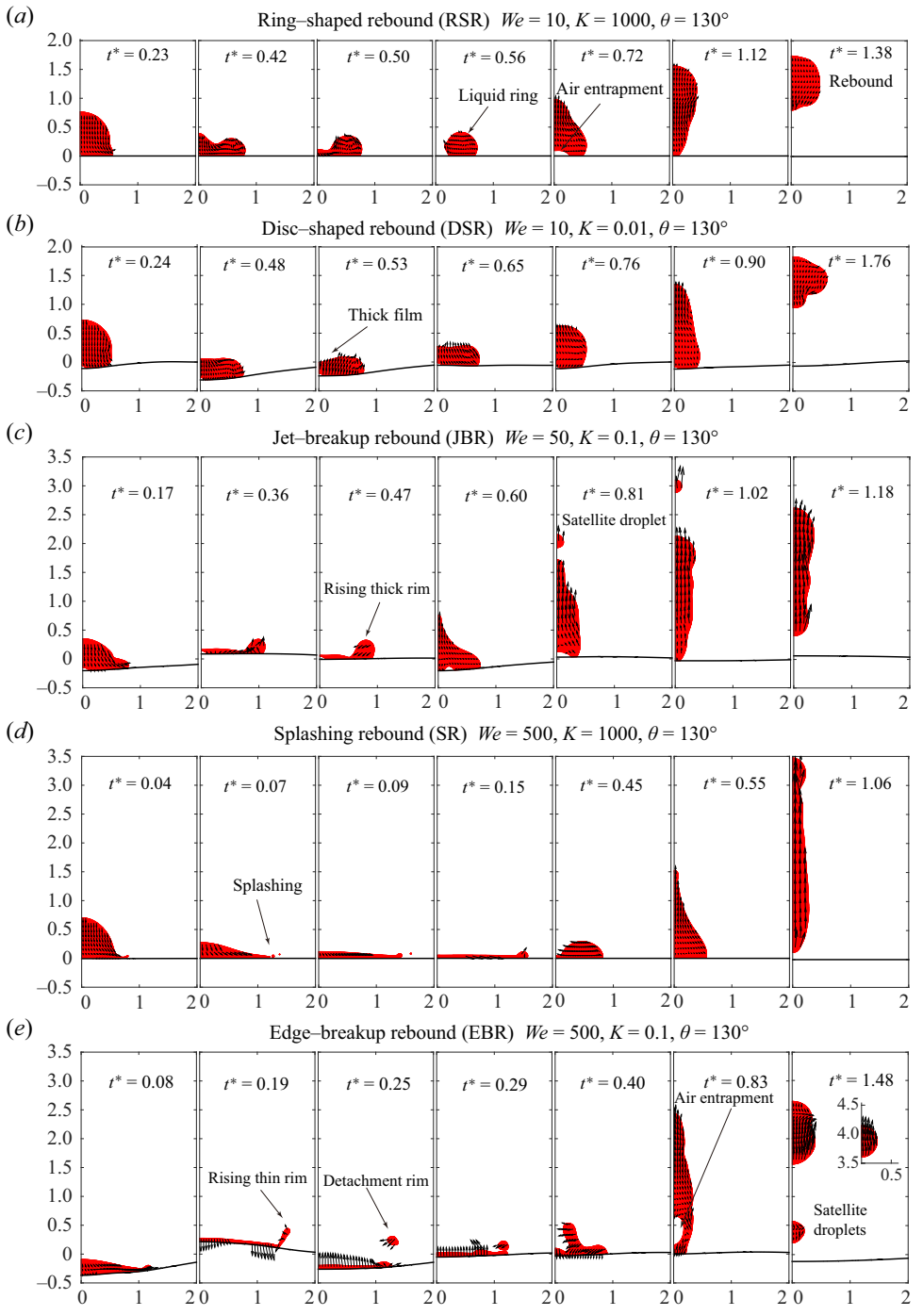

Figure 5. Snapshots of a droplet impacting on a flexible substrate for typical cases: (*a*) $We = 10$ and $K = 1000$; (*b*) $We = 10$ and $K = 0.01$; (*c*) $We = 50$ and $K = 0.1$; (*d*) $We = 500$ and $K = 1000$ and (*e*) $We = 500$ and $K = 0.1$, corresponding to the RSR, DSR, JBR, SR and EBR modes, respectively.

The contraction of the liquid ring leads to the regeneration and the complete rebound of the droplet.

For the case where $We = 10$ and $K = 0.01$, corresponding to the DSR mode as shown in figure 5(*b*), the kinetic energy of the droplet is partially converted into the deformation energy and kinetic energy of the flexible substrate, which leads to a smaller effective *We* number for droplet impact. Therefore, compared with the case where $We = 10$ and $K = 1000$ (figure 5*a*), the formation of liquid ring is not observed during the droplet spreading stage; instead, the droplet evolves into a disc-like morphology in the late stage of spreading. Compared with the rigid case, when the flexible substrate moves upwards, partial energy of the substrate is converted into the kinetic energy of the droplet, resulting in a liquid film that has an upward velocity (at $t^* = 0.65$), which does not appear in the previous example.

For the case where $We = 50$ and $K = 0.1$, corresponding to the JBR mode as shown in figure 5(*c*), a thin liquid film and thick rim are formed at the centre and the outer edge, respectively. Due to the lager *We*, spreading will cause the accumulation of the liquid medium at the edges of the droplet. As the substrate rebounds, the edges of the droplet acquire upward velocity, resulting in the conversion of the kinetic energy to the surface energy. This leads to a slight longitudinal stretching and a contraction of the contact line at the edges, partially detaching from the substrate and forming a rising thick rim (at $t^* = 0.47$). After merging, there is a tendency for jetting, resulting in the detachment of a small satellite droplet from the main body of the droplet at the tip (at $t^* = 0.81$). The detached satellite droplet has a greater rising velocity than the main body of the droplet detaching from the substrate.

For the case where $We = 500$ and $K = 1000$, corresponding to the SR mode as shown in figure 5(*d*), after the impact, a non-wetting thin lamella appears at the edge of the droplet (at $t^* = 0.04$). Under the effect of high *We*, the surface tension is not sufficient to restrain the rapid spreading of the droplet. The capillary instability occurs, making the droplet experience a prompt splashing (at $t^* = 0.07$).

For the case where $We = 500$ and $K = 0.1$, corresponding to the EBR mode as shown in figure 5(*e*), due to the absorption of a portion of the droplet's kinetic energy by the substrate, splashing does not occur although the Weber number is equal to that for the case in figure 5(*d*) (at $t^* = 0.08$). This phenomenon is similar to the findings of Howland *et al.* (2016). However, during the subsequent substrate rebound, the thin lamella at the edge acquires an upward velocity, leading to longitudinal stretching, while the contact line retracts. When the substrate reaches its maximum height and starts moving downward, the moving direction of the thin lamella is opposite to that of the central liquid film (at $t^* = 0.19$). This intensifies the longitudinal stretching of the thin lamella, eventually leading to the necking phenomenon and the separation of a liquid ring from the main film. After separation, under the effect of surface tension, the liquid ring begins to contract towards the centre and merges with the liquid film on the rising substrate (at $t^* = 0.29$). The merging process creates a local protrusion on the film during retraction (at $t^* = 0.40$), and the ring-shaped protrusion moves to the centre and finally encloses with an air bubble trapped (at $t^* = 0.83$). The merged droplet longitudinally stretches and undergoes necking due to the velocity differences at different heights. Eventually, the liquid column separates into multiple satellite droplets of varying sizes.

The distribution of the above five modes in a parameter space (*We*, *K*) is shown in figure 6. The intact rebound (IR, e.g. RSR or DSR) occurs at $1 \leq We \leq 10$, while the breakup rebound (BR, e.g. JBR, SR and EBR) occurs at $25 \leq We \leq 500$.

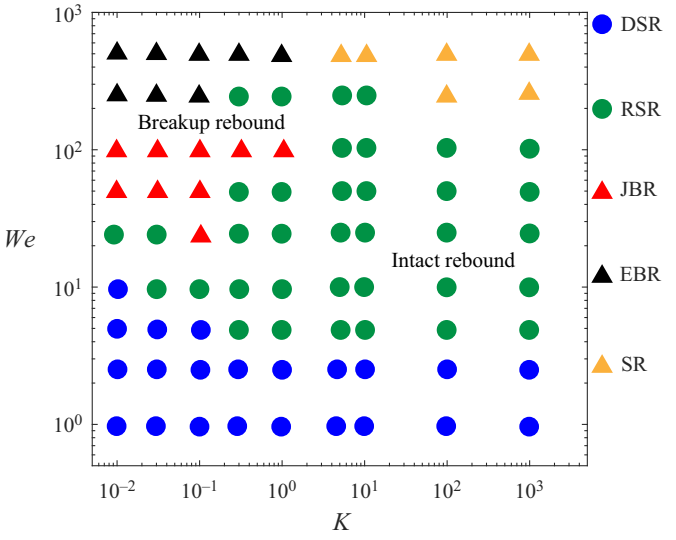

Figure 6. Five impact modes in a parameter space (K, We) for $\theta = 130°$. Circles and triangles denote the intact rebound (IR) and breakup rebound (BR), respectively. Green circles, blue circles, red triangles, orange triangles and black triangles denote the ring-shaped rebound (RSR), the disc-shaped rebound (DSR), the jet-breakup rebound (JBR), the splashing rebound (SR) and edge-breakup rebound (EBR), respectively.

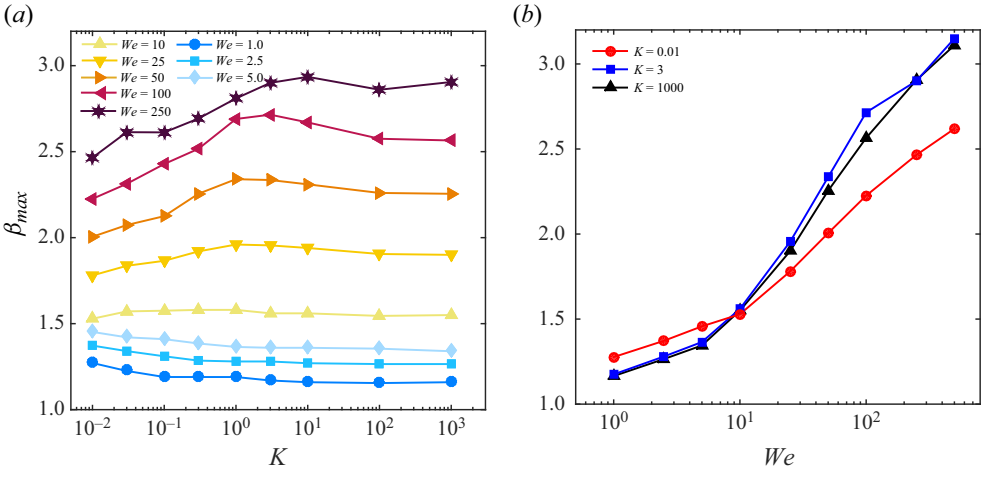

Figure 7. Variation of the maximum spreading factor β_{max} (a) with K for different We and (b) with We for different K.

3.2. *Maximum spreading factor and spreading time*

Regarding the droplet impact on a solid surface, the maximum spreading factor has always been a research hotspot. In the following, we will focus on the effect of the substrate flexibility on the maximum spreading factor (β_{max}).

From figure 7(a), it can be observed that as K gradually decreases, β_{max} exhibits two opposite trends for $We < 10$ and $10 < We \leq 250$, respectively. For the low-We region ($We < 10$), as K decreases from 1000 (rigid) to 0.01 (very flexible), β_{max} shows a weak increasing trend. While for the higher We region ($10 < We \leq 250$), β_{max} first shows a

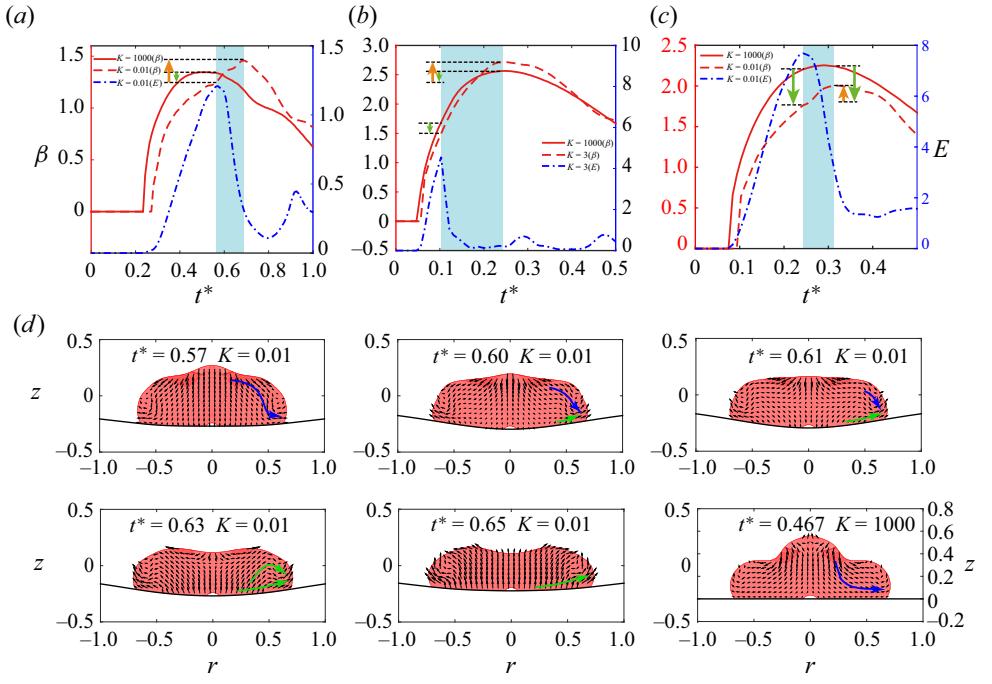

Figure 8. Spreading factor for the cases at (*a*) $We = 5$ and $K = 0.01$ and 1000, (*b*) $We = 100$, $K = 3$ and 1000, and (*c*) $We = 50$, $K = 0.01$ and 1000. The blue dash-dotted line represents the total energy of the substrate. The orange and green arrows indicate the relative increase and reduction of the spreading factor during the substrate's downward and upward motions, respectively. The shaded regions in panels (*a*), (*b*) and (*c*) correspond to the time interval from the moment when the substrate energy reaches its peak to the moment when the droplet achieves maximum spreading. (*d*) Snapshots of the droplet during the shaded region for $K = 0.01$ in panel (*a*). The lower right corner is a snapshot of the droplet at the eve of maximum spread at $K = 1000$. The blue and green arrows indicate two different flows.

slight increase when K decreases from 1000 to 1, and then decreases significantly when K further decreases from 1 to 0.01. The variation trend of β_{max} with K for $10 \leq We \leq 250$, $0.01 \leq K \leq 1$ is consistent with those reported by Ma & Huang (2023). The weakened spreading induced by the substrate flexibility is attributed to the fact that the disk absorbs a part of the droplet's kinetic energy for spreading. In contrast, it is observed in figure 7(*a*) that β_{max} slightly increases as K decreases for $1 \leq We \leq 5$ and $0.01 \leq K \leq 1$. This spreading enhancement due to the substrate flexibility has not been reported by Ma & Huang (2023) or in other relevant studies. Figure 7(*b*) shows the β_{max} as a function of We for the cases of $K = 0.01$, 3 and 1000, providing a clearer demonstration of the trends in β_{max}. It is obvious that the spreading enhancement (weakness) occurs for $K = 0.01$, $We < 10$ ($We > 10$). Figure 8(*a*) demonstrates the time variation curves of the spreading factor β for $We = 5$ and $K = 0.01$, 1000. Compared with the rigid case ($K = 1000$), there is a time lag in the rise of the curve for the case with $K = 0.01$, due to the wetting hysteresis caused by the downward movement of substrate. As the substrate moves downward, the β is smaller than that for the rigid case in the early stage of droplet spreading. However, as the substrate moves upward, β reaches the maximum value which is larger than that for the rigid case. To understand the changing of the spreading factor, figure 8(*d*) shows the snapshots from the moment of maximum substrate energy to the moment of maximum spreading factor for the case with $We = 5$, $K = 0.01$, contrasted with the snapshot for the rigid case at the

certain moment ($t^* = 0.467$) before reaching β_{max}. At $t^* = 0.57$, due to impacting, the liquid inside the droplet flows from the top to the edge (marked with a blue arrow in figure 8*d*). As the substrate moves upward, it compresses the bottom of the droplet, and at $t^* = 0.60$ as shown in figure 8(*d*), both the top and bottom parts of droplet exhibit a tendency to flow to the edge. The flow at the top part becomes weaker, while the flow at the bottom part (marked with a green arrow in figure 8*d*) becomes stronger as the droplet spreads. After $t^* = 0.63$, the flow to the edge is entirely driven by the upward movement of the substrate. Therefore, the larger β_{max} at $K = 0.01$ compared with the rigid case is caused by the upward motion of the substrate in the late stage of droplet spreading. In conclusion, compared with the rigid case, the squeezing effect of substrate on the droplet caused by the substrate's upward movement contributes to the droplet spreading, which is manifested by the extension of spreading time and the increase of the maximum spreading factor.

Accordingly, the variations of the spreading factor in figure 8(*b*,*c*) can be explained. For figure 8(*b*), the difference from figure 8(*a*) is that higher bending stiffness leads to faster oscillation, resulting in the moment of the first downward and upward movement of substrate being significantly earlier than the moment of the maximum spreading. In this case, the squeezing of the substrate on the droplet makes the maximum spreading factor of the droplet increase, but has no obvious effect on the spreading time. For figure 8(*c*), spreading enhancement caused by the substrate's upward movement is smaller than spreading weakening caused by the substrate's downward movement, Therefore, the net changes in the maximum spreading factor for $K = 0.01$ are negative, i.e. the maximum spreading factor decreases compared with that for the rigid case.

It is noted that the differences between the present study and the study of Ma & Huang (2023) are the vibration behaviour of the substrate. In the present study, the substrate vibration is affected by both *We* and *K*, which is slightly different from that observed by Ma & Huang (2023). In the present study, the moment of the first valley of the substrate deflection curve occurs always earlier than the moment of maximum spreading factor. However, the moment of the first valley of the substrate deflection curve can be earlier or later than the moment of maximum spreading factor reported by Ma & Huang (2023). This difference may be attributed to the different types of the substrates. In our study, a disc-shaped substrate with edge support is used. Additionally, the different parameter scopes considered may also have an influence.

The analysis above clarifies why β_{max} is greater or smaller than that for the rigid substrate cases. However, it does not fully explain the trends of β_{max} observed in figure 7(*b*). To address this point, we quantify the decreasing and increasing effects on the spreading factor during the downward and upward stage of the substrate. The relative spreading weakening caused by the downward movement and the relative spreading enhancement caused by the upward movement, i.e. $\Delta\beta_1$ (note that $\Delta\beta_1 < 0$) and $\Delta\beta_2$, are defined, respectively. These quantities are indicated by the green and orange arrows in figure 8(*a–c*), respectively. Thus, the net change in spreading factor, $\Delta\beta = \Delta\beta_1 + \Delta\beta_2$.

Figure 9 shows the changes in the spreading factor as a function of *We* for $K = 0.01$ and $K = 3$. As shown in figure 9(*a*), as *We* increases, the spreading weakens, i.e. $|\Delta\beta_1|$, gradually increases due to the increasing impact energy; however, the spreading enhancement, i.e. $\Delta\beta_2$, has no significant change. There are possible reasons for these observations. As mentioned above, $\Delta\beta_2$ is caused by the upward movement of the substrate. Thus, a higher *We* does not necessarily imply greater $\Delta\beta_2$ during the upward movement. Whether the droplet continues to spread or retract during the upward stage of the substrate depends on the relative magnitude between droplet kinetic energy and surface

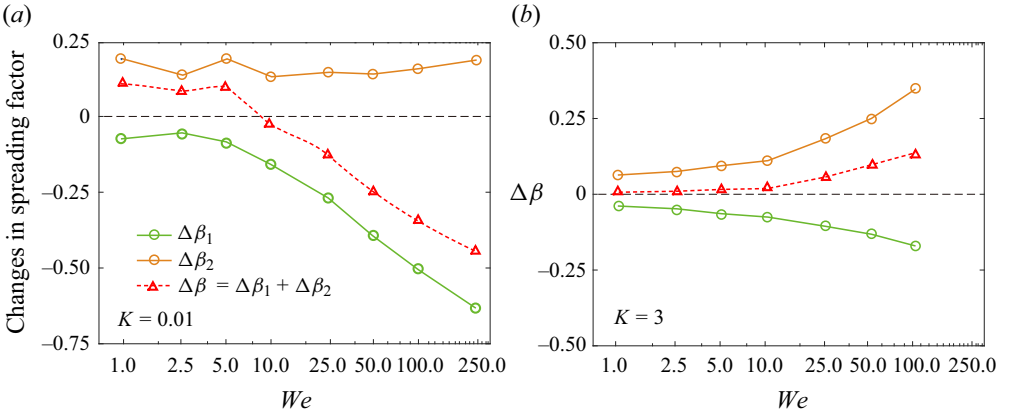

Figure 9. Relative weakening ($\Delta\beta_1$) and enhancement ($\Delta\beta_2$) of spreading factor caused by substrate's downward and upward movement, as well as the net effect ($\Delta\beta$), for two bending stiffness: (*a*) $K = 0.01$ and (*b*) $K = 3$.

energy. However, it is obvious that as *We* increases, a larger initial impact energy of the droplet will promote the downward movement of the substrate, which results in a larger $\Delta\beta_2$. The different trends of curves for $\Delta\beta_1$ and $\Delta\beta_2$ result in $\Delta\beta$ being positive when $We < 10$ and negative when $We > 10$, which corresponds to the spreading enhancement and weakening.

For the cases for $K = 3$ shown in figure 9(*b*), both the spreading enhancement and spreading weakening increase as *We* increases. The spreading enhancement is slightly larger than the spreading weakening, resulting in the positive $\Delta\beta$ which increases with *We*. This indicates that the spreading enhancement due to the substrate rebound dominates the droplet spreading for the high-*We* region.

Based on the previous analysis, the upward movement of the substrate during the late spreading stage may prolong the spreading stage. The spreading time, $T_{\beta_{max}}$, represents the duration from when the droplet begins to contact the substrate until it achieves maximum spreading. Figure 10 illustrates the variation of $T_{\beta_{max}}$ with *We* and *K*. Only for $We \leq 25$, the spreading time gradually increases with the decreasing *K*, particularly for $K \leq 10$; while for $We > 25$, $T_{\beta_{max}}$ remains almost constant with *K*.

3.3. *Scaling law*

The maximum spreading factor (β_{max}) describes the maximum extent of spreading of a liquid droplet upon impact with a solid surface. It is crucial for understanding the interaction between the droplet and the surface, making it an important physical quantity for characterising the dynamics of droplet impact on surfaces. Therefore, how to theoretically predict β_{max} is a question of widespread interest.

For the case of a liquid droplet impacting a rigid wall, various theoretical prediction models for β_{max} have been developed based on the conversion relationship among droplet kinetic energy, viscous dissipation and surface energy. For example, in the viscous regime where inertial and viscous forces dominate, research by Chandra & Avedisian (1991) indicates $\beta_{max} \sim Re^{1/5}$; while in the capillary regime where viscosity may be neglected, Collings *et al.* (1990) obtain another scaling law, $\beta_{max} \sim We^{1/2}$, by assuming that all the kinetic energy is transformed into surface energy at the maximal spreading. However, an alternative scaling has been suggested for the same regime. Based on momentum

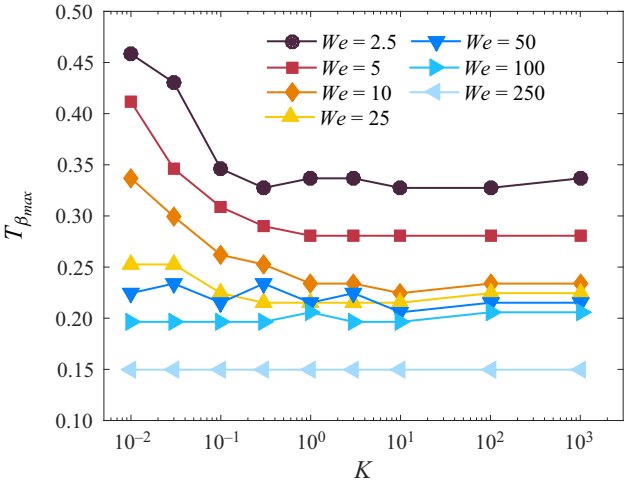

Figure 10. Effect of K on the spreading time $T_{\beta_{max}}$ for different We.

conservation, Clanet *et al.* (2004) proposed that $\beta_{max} \sim We^{1/4}$. In more scenarios, the influences of viscous dissipation or surface tension on spreading cannot be simply excluded, otherwise it will result in the breakdown of the above scaling laws. By interpolating between the $We^{1/2}$ and $Re^{1/5}$ scaling, Eggers *et al.* (2010) showed that in the cross-over regime between capillary and viscous regimes, $\beta_{max} \propto Re^{1/5} f_c(P)$, where f_c is a function of the impact parameter P ($= We\, Re^{-2/5}$) that varies between zero (capillary regime) and infinity (viscous regime). Further, Laan *et al.* (2014) constructed the smooth cross-over between these two asymptotes by using a so-called Padé approximant, i.e. $\beta_{max} Re^{-1/5} = P^{1/2}/(A + P^{1/2})$, where A is a fitting constant. Lee *et al.* (2016) extended Laan's approach (Laan *et al.* 2014) by considering wettability. It is found that, after a correction for dynamic wetting using the maximum spreading ratio at zero velocity $\beta_{V\to 0}$, the maximum spreading should still scale with $We^{1/2}$, i.e. $(\beta_{max}^2 - \beta_{V\to 0}^2)^{1/2} \sim We^{1/2}$. Building on this conclusion, and considering that Re is constant in this study, a universally applicable prediction model of β_{max} can be derived by following Laan's approach:

$$(\beta_{max}^2 - \beta_{V\to 0}^2)^{1/2}\, Re^{-1/5} = \frac{We^{1/2}}{B + We^{1/2}}, \tag{3.1}$$

where B is a fitting coefficient which may vary across different Re cases. However, in the present study, B is considered a constant coefficient due to the fixed value of Re. Also, $\beta_{V\to 0}$ can be calculated from the contact angle (Lee *et al.* 2016),

$$\beta_{V\to 0} = \begin{cases} \left(\dfrac{4\sin^3\theta_{V\to 0}}{2 - 3\cos\theta_{V\to 0} + \cos^3\theta_{V\to 0}}\right)^{1/3} & \text{if } \theta_{V\to 0} < 90^\circ, \\ \left(\dfrac{1}{(2+\cos\theta_{V\to 0})\sin^4(\theta_{V\to 0}/2)}\right)^{1/3} & \text{if } \theta_{V\to 0} > 90^\circ. \end{cases} \tag{3.2}$$

For flexible substrate scenario, theoretical predictions of β_{max} become more challenging because vibration and deformation of substrate will significantly affect the spreading of a droplet. Based on Lee *et al.*'s (2016) theoretical model for rigid substrate cases, Ma & Huang (2023) have proposed a scaling law of β_{max} for a droplet impacting on a flexible

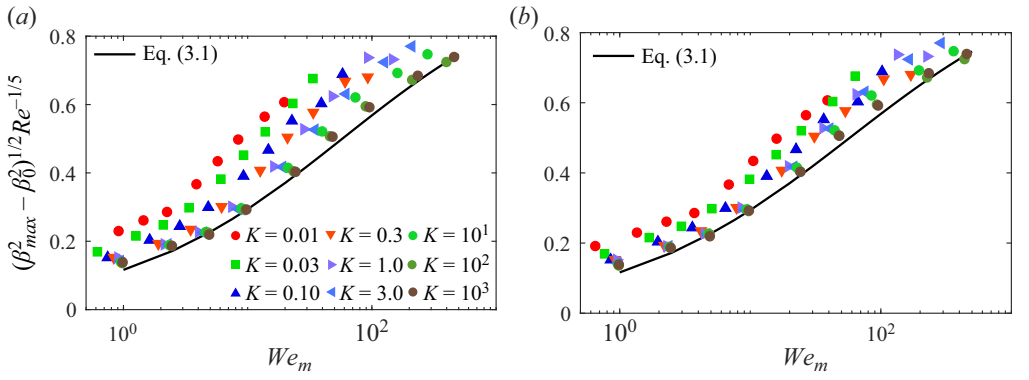

Figure 11. The $\beta_m=(\beta_{max}^2-\beta_0^2)^{1/2}Re^{-1/5}$ as a function of We_m for varying stiffness K. (*a*) We_m is calculated by the theoretical natural frequency of the Euler–Bernoulli beam f_0; (*b*) We_m is calculated based on the natural frequency of the present shell obtained through numerical experiments. The solid line is plotted by (3.1) and B is 7.6.

plate simply supported at its both edges, by defining an effective Weber number, i.e.

$$We_m=\frac{We}{1+\delta_{max}}, \tag{3.3}$$

where δ_{max} is the substrate deflection. Due to momentum conservation, δ_{max} can be predicted as

$$\delta_{max}=\frac{1}{2\pi}\frac{m}{m+M_s/3}\frac{U_0}{fD_0}, \tag{3.4}$$

in which m and M are the mass of the droplet and the flexible substrate, respectively, U_0 is the initial velocity of the droplet, $f=f_0[M_s/(m+M_s)]^{1/2}$ is the vibration frequency of the system, and $f_0=\pi\sqrt{EI/M_sL^3}/2$ is the natural vibration frequency of a simple-support Euler–Bernoulli beam on both ends. The effective Weber number We_m takes all the factors affecting β_{max} into account.

Following the prediction model for β_{max} proposed by Ma & Huang (2023), the numerical results obtained in the present study have been plotted in the $We_m-\beta_m$ plane, where $\beta_m=(\beta_{max}^2-\beta_0^2)^{1/2}Re^{-1/5}$ and $\beta_0=\beta_{V\to0}$, as shown in figure 11. In figure 11(*a*), the effective Weber number We_m is calculated by the theoretical natural frequency of the Euler–Bernoulli beam f_0; the data symbols are spread over the parametric plane for varying K, indicating a poor data collapse. The reason is that the natural frequency of the shell in the present study cannot be accurately predicted with f_0. Since it is difficult to predict the natural frequencies of shells theoretically, we determine the natural frequencies of shells with different stiffnesses K through numerical experiments. As shown in figure 11(*b*), when the numerically measured natural frequencies of the shells are used to predict We_m by (3.3)–(3.4), the data collapse together. Also, we can see that all data distribute above the solid line plotted by (3.1), indicating that the We_m is slightly underestimated. This is because the maximum deflection δ_{max} is no longer the only characteristic quantity that defines We_m due to the emergence of distinct mechanisms of shell–droplet coupling in the present problem. In the following, according to the revealed physical mechanisms, We_m has been modified to seek a better data collapse.

From the analysis of figures 8 and 9, the spreading process of a droplet on a flexible substrate can be divided into two stages. The first stage is from when the droplet starts

to contact the substrate until the substrate energy reaches the maximum. In this stage, the energy is transferred from the droplet to the substrate which continues to dent downward. In the second stage, from when the substrate energy reaches the peak until the droplet reaches its maximum spreading, the substrate continues to rebound and the substrate energy is transferred to the droplet.

During the first stage, the effective Weber number decreases due to the depression of the substrate and thus the droplet spreading is suppressed; while during the second stage, the effective Weber number increases due to the rebound of the substrate and the droplet spreading is promoted. Therefore, the effect of flexible substrate on the maximum spreading factor depends on the competition of these two mechanisms. Specifically, when $|\Delta\beta_1| < \Delta\beta_2$ (see figure 8*a*,*b*), $\Delta\beta = \Delta\beta_1 + \Delta\beta_2 = \Delta\beta_2 - |\Delta\beta_1| > 0$, indicating spreading enhancement dominated by the 'flexible rebound mechanism'; while when $|\Delta\beta_1| > \Delta\beta_2$ (see figure 8*c*), $\Delta\beta = \Delta\beta_1 + \Delta\beta_2 = \Delta\beta_2 - |\Delta\beta_1| < 0$, indicating spreading suppression dominated by 'flexible compliant mechanism'. It is worth noting that the spreading suppression dominated by the flexible compliant mechanism has been found in previous studies (Vasileiou *et al.* 2016; Xiong *et al.* 2020; Ma & Huang 2023); however, the spreading enhancement caused by the flexible rebound mechanism has not been reported before.

In the scaling law proposed by Ma & Huang (2023), the maximum deflection δ_{max} has been used to correct the *We*, that is, (3.3), which is appropriate for the region where the flexible compliance mechanism dominates. However, in the region where the flexible rebound mechanism dominates, the effective Weber number increases and is related to the rebound displacement of the substrate, δ_{reb}, and thus (3.3) is no longer applicable. Instead, δ_{reb} has been used to predict the effective Weber number (We_m), i.e. $We_m = We/(1+\delta_{reb})$ for $\Delta\beta > 0$. Therefore, (3.3) is modified to

$$We_m = \frac{We}{1+\delta}, \quad \delta = \begin{cases} \delta_{max} & \text{if } \Delta\beta > 0, \\ \delta_{reb} & \text{if } \Delta\beta < 0, \end{cases} \tag{3.5}$$

where δ_{reb} (note that $\delta_{reb} < 0$) and δ_{max} can be obtained from the numerical results. Based on the modified We_m calculated by (3.5), it is shown in figure 12 that $\beta_m = (\beta_{max}^2 - \beta_0^2)^{1/2} Re^{-1/5}$ as a function of We_m for varying stiffness K. It is seen that all data are collapsed on the same solid line plotted by (3.1), indicating that the modified We_m calculated by using (3.5) leads to a better data collapse compared with those in figure 11(*a*,*b*).

3.4. *Impact force*

According to the study by Zhang *et al.* (2022) on the impact force for a droplet impacting on a superhydrophobic rigid surface, an inertial shock will lead to the appearance of the first peak of the impact force when the maximum droplet diameter is approximately equal to the initial diameter. The magnitude of this peak is independent of the wettability of the surface. When the droplet retracts, the momentum conservation results in the formation of an upward jet as well as an internal downward jet, which leads to the appearance of the second force peak. However, few studies on the time variation of impact force for flexible substrate situations have been reported. In this section, we focus on the impact force during droplet impact on flexible substrates.

Figure 13(*a*) makes a comparison between the previous experimental and present numerical results. The parameters in the simulations are identical to those of Zhang *et al.*'s (2022) experiments, except for the contact angle of the substrate. For the same reasons

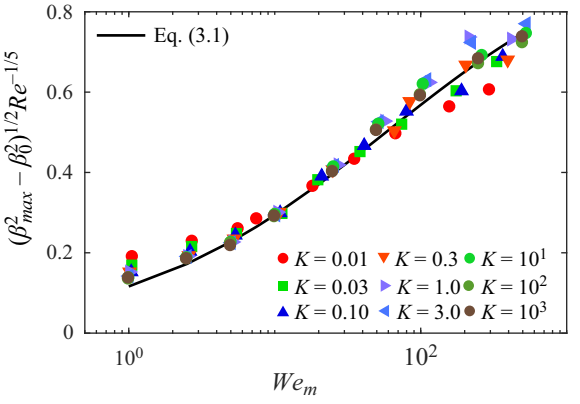

Figure 12. The $\beta_m = (\beta_{max}^2 - \beta_0^2)^{1/2}Re^{-1/5}$ as a function of We_m for varying stiffness K. The modified We_m is calculated by (3.5).

mentioned as in § 2.3, a static contact angle of 130° is used in the simulations. As shown in figure 13(*a*), the timing and amplitude of the first force peak in the simulations coincide generally with the results from Zhang *et al.* (2022). The impact force reaches a valley near the moment of maximum spreading, before the appearance of the second force peak in the retraction stage of the droplet. The occurrence of the three characteristic moments (corresponding droplet shape snapshots are given in figure 13*a*) is consistent with the report of Zhang *et al.* (2022). The difference in the contact angle may be responsible for the difference in the valley value of the impact force and the timing of the second peak. The impact force for $K = 1000$ almost overlaps with that for the rigid case, indicating that the calculation of impact force in our model is reliable.

Further, we select the cases with $K = 0.1$, $We = 5$, 50 and 500 for impact force analysis, which are shown in figures 13(*b*)–13(*d*), respectively. For comparison, we calculate the impact forces on a rigid substrate under the same parameters. However, in some cases with $K = 1000$, the substrate exhibits subtle high-frequency vibrations, which result in severe spikes in the curve of the impact force. Thus, it is not suitable to approximate the substrate with $K = 1000$ as a rigid substrate for comparison. In this case, we directly compare the impact forces on the flexible substrates with that on the rigid wall.

For the case with $We = 5$ in figure 13(*b*), the observed slope changes in the deflection curve in figure 13(*b*) correspond to the peak and valley of the impact force. Compared with the rigid substrate cases, the impact force curve for the flexible substrate exhibits more frequent fluctuations. During the time period from $t^* = 0.2$ to $t^* = 0.4$, the substrate undergoes the downward movement due to the droplet impact, resulting in a lower impact force on the flexible substrate compared with the rigid wall at the same time. At the moment of two deflection valleys, the impact force reaches two prominent peaks, which are significantly larger than those on the rigid wall.

It can be observed from figure 13(*c*) that, similar to the case of $We = 5$, significant peaks of the impact force occur at the two moments corresponding to the valleys of the deflection curve for $We = 50$. However, in this case, the substrate undergoes upward deflection beyond its initial position during the upward movement stage. As the substrate moves upward, the impact force rapidly decreases, changing from positive to negative, and then reaches a valley near the moment of the deflection peak. This indicates that the effect of the droplet on the substrate gradually shifts from compression to adsorption as the

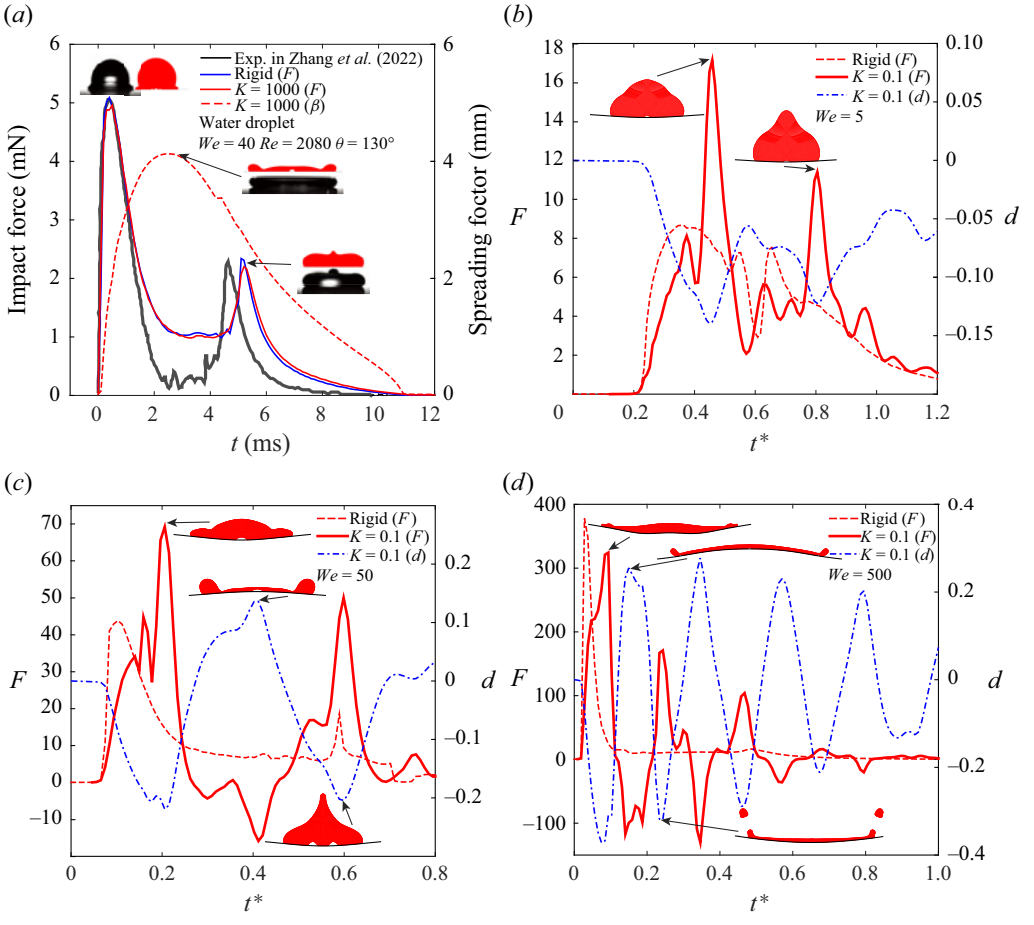

Figure 13. (*a*) Validation of impact force on the substrate: the thick solid black line represents the experimental results from Zhang *et al.* (2022), the blue and red solid lines represent the simulation results on the rigid substrate and the substrate with $K = 1000$, and the red dashed line represents the spreading factor. Evolution of impact force for (*b*) $We = 5$ and $K = 0.1$, (*c*) $We = 50$ and $K = 0.1$ and (*d*) $We = 500$ and $K = 0.1$. In panel (*b–d*), the blue dashed line represents the deflection curve of the substrate, the thick solid red line represents the impact force on the flexible substrate and the red dashed line represents the impact force on the rigid substrate. Each arrow points to the moment corresponding to the snapshot of the droplet.

substrate moves upward beyond its initial position, which is a phenomenon not observed in the case of impacting on a rigid wall.

As shown in figure 13(*d*), when *We* increases to 500, the substrate exhibits strong oscillations near the equilibrium position at a higher frequency, which leads to alternating peaks and valleys in the load curve, corresponding to the valleys and peaks of the substrate deflection curve, respectively.

3.5. *Energy conversion*

When a droplet impacts on a hydrophobic rigid wall, the conversion of the kinetic energy of the droplet and its surface energy plays an important role in spreading dynamics of the droplet. However, when the substrate is flexible, it is evident that the energy of the substrate (including the elastic strain energy and the kinetic energy) participates in the energy conversion. In this section, we will discuss the energy conversion in the

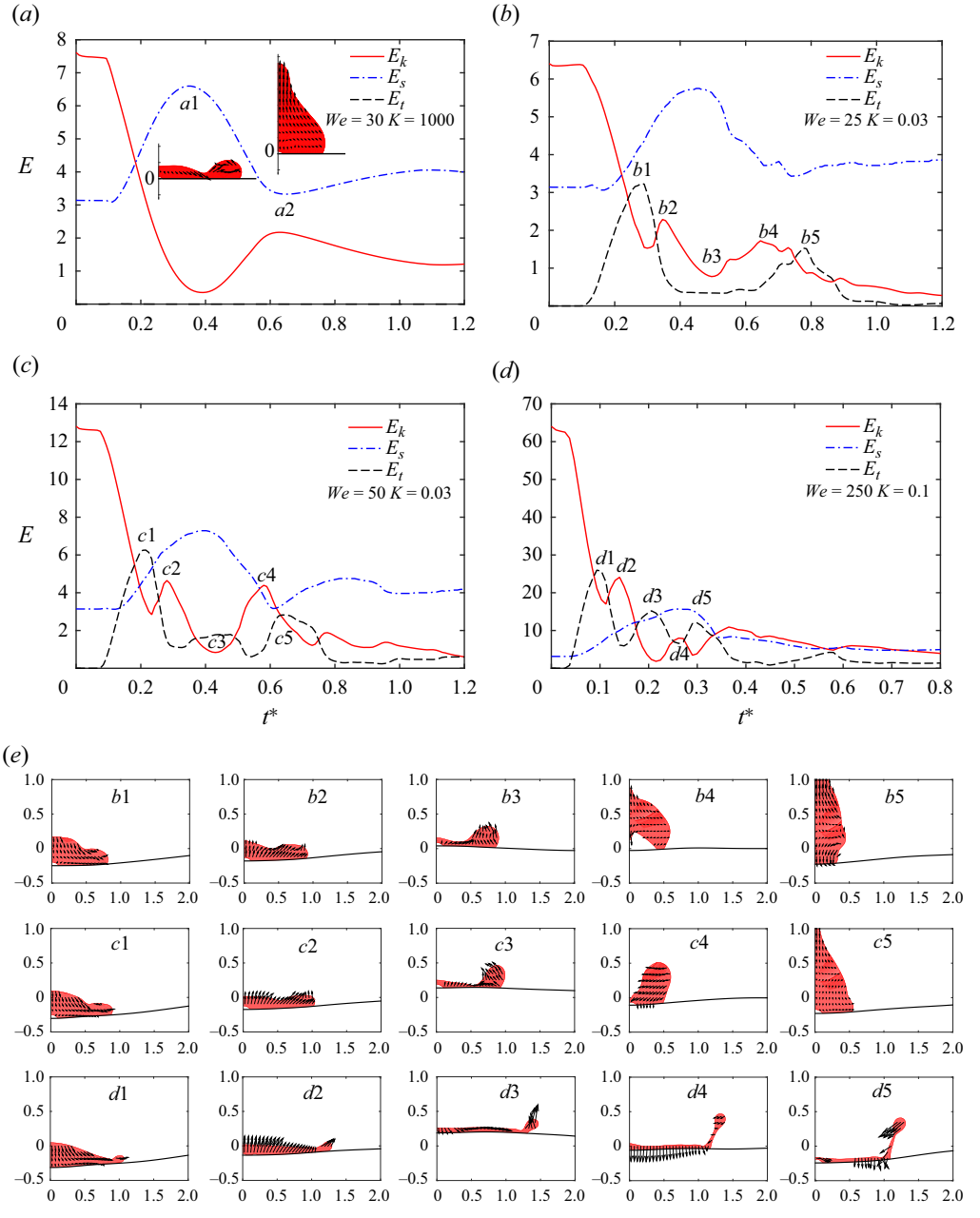

Figure 14. Time evolution of energy for four typical cases: (*a*) $We = 30$ and $K = 1000$; (*b*) $We = 25$ and $K = 0.03$; (*c*) $We = 50$ and $K = 0.03$ and (*d*) $We = 250$ and $K = 0.1$, and (*e*) corresponding snapshots at labelled moments in panel (*b–d*). In panel (*a–d*), the red solid, blue dash-dotted and black dashed lines represent the droplet's kinetic energy (E_k), the droplet's surface energy (E_s) and the total energy of the substrate (E_t), respectively.

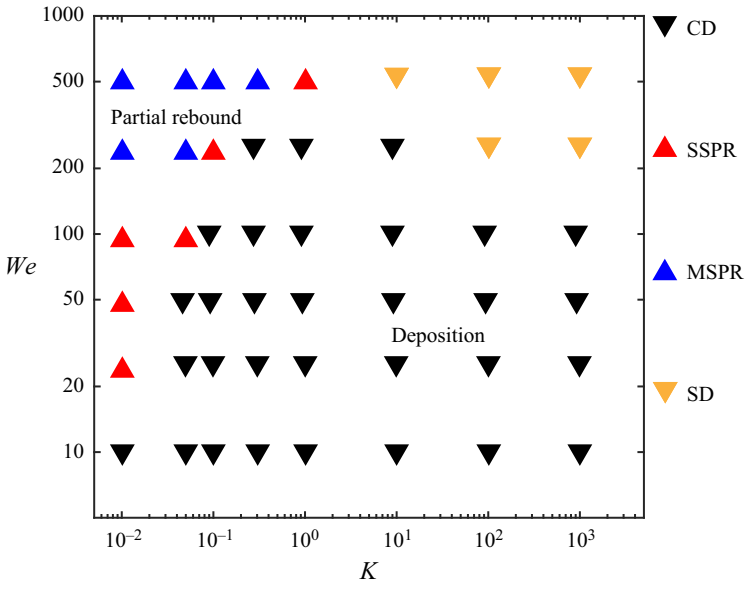

Figure 15. Four impact modes in a parameter space (K, We) for $\theta = 60°$. Black down-pointing triangles, orange down-pointing triangles, red up-pointing triangles and blue up-pointing triangles denote the complete deposition (CD), splashing deposition (SD), single-satellite partial rebound (SSPR) and multi-satellites partial rebound (MSPR) modes, respectively.

droplet–substrate coupling. We focus on the interaction between the kinetic energy of the droplet (E_k), the surface energy (E_s) and the total energy of the substrate (E_t). In the present simulations, E_t is calculated by the sum of the substrate kinetic energy and potential energy, $E_k = \frac{1}{2}\int \rho v^2 \,\mathrm{d}V$ and $E_s = \sigma(A_{LV} - A_{SL}\cos\theta)$, where A_{LV} and A_{SL} are the liquid–vapor and liquid–solid contact area, respectively (Du *et al.* 2021).

The typical processes of the energy interaction are summarised in figure 14. For comparison, figure 14(*a*) shows the time variations of E_k and E_s for $K = 1000$ (rigid case), where the substrate energy does not participate in the energy interaction. Figures 14(*b*)–14(*d*) show the three typical energy interaction processes, respectively, while the corresponding snapshots at key moments are shown in figure 14(*e*). These energy interaction processes correspond basically to the three types of changes in impact force in figure 13. As shown in figure 14(*b*), after impact, E_k starts to convert into E_s and E_t. At $t^* = b_1$, the substrate deflection reaches a peak and, subsequently, the upward motion of the substrate induces an upward velocity of the droplet, resulting in a small increase of droplet kinetic energy (E_k). Near $t^* = b_3$, E_s reaches the maximum and the substrate is near its initial position, leading to E_t approaching zero. Subsequently, the droplet starts to retract and E_s is converted back into E_k. At the moment $t^* = b_4$, E_k reaches another peak. During retraction, the downward momentum within the droplet leads to another impact on the substrate, resulting in the conversion of E_k into E_t. At $t^* = b_5$, E_t reaches the second peak; meanwhile, the deflection reaches a peak. The occurrences of two peaks of E_t (b_2 and b_5) are attributed to the initial impact and the subsequent retracting impact, respectively. In figure 14(*c*), it is shown that after passing the initial position, the droplet briefly adsorbs the substrate and moves upward for a distance (see figure 13*c*), which results in the conversion of E_k into E_t and E_s, and the second peak of E_t appears at $t^* = c_3$. The subsequent changes in the energies are similar to those in figure 14(*b*). In this case, E_t exhibits three peaks

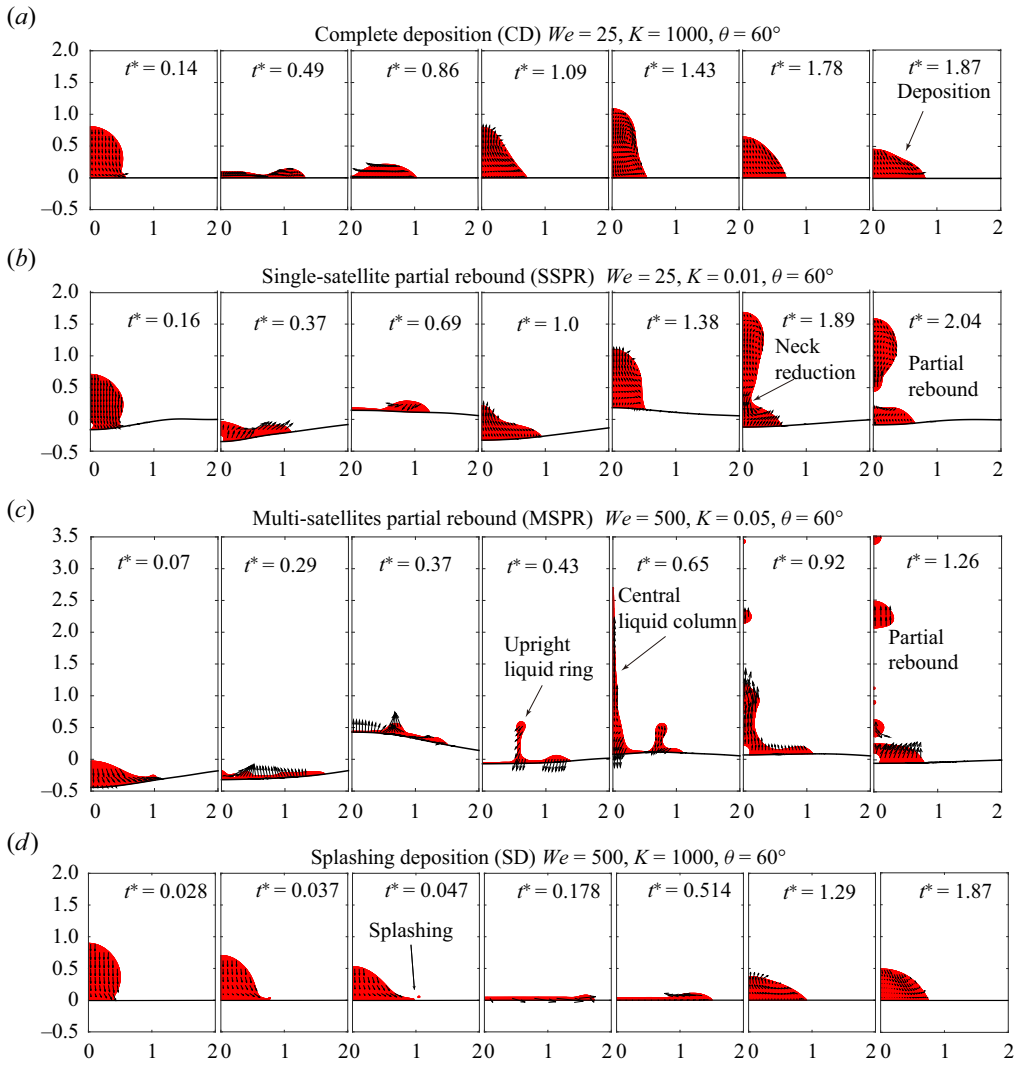

Figure 16. Snapshots of typical cases for four impact modes: (*a*) $We = 25$ and $K = 1000$; (*b*) $We = 25$ and $K = 0.01$; (*c*) $We = 500$ and $K = 0.05$; and (*d*) $We = 500$ and $K = 1000$, corresponding to the CD, SSPR, MSPR and SD modes, respectively.

due to the short absorption of the droplet to the substrate. Figure 14(*d*) shows the mutual conversion between E_k and E_s, which corresponds to the results in figure 13(*d*).

3.6. *Impact dynamics on hydrophilic substrates*

To investigate the effect of hydrophilic substrates on the droplet impact dynamics, we set the contact angle to 60°. Figure 15 shows the impact modes in a parameter space (K, We) for $\theta = 60°$. According to whether the droplet completely deposits on the substrate, the impact modes are classified into two main types: deposition (DP) and partial rebound (PR), corresponding to the down-pointing and up-pointing triangles in figure 15, respectively. Based on the droplet shape evolution, we can subdivide the DP mode into complete deposition (CD) and splashing deposition (SD). For the PR mode, we can subdivide it into single-satellite partial rebound (SSPR) and multi-satellites partial rebound (MSPR).

Figure 16 presents snapshots for the typical case for each mode. For the case where $We = 25$ and $K = 1000$ (see figure 16*a*), corresponding to the CD mode, the droplet is ultimately deposited on the substrate (at $t^* = 1.87$) after a period of oscillations.

For the case where $We = 25$ and $K = 0.01$ (see figure 16*b*), corresponding to the SSPR mode, it is shown that the obvious difference from the case in figure 16(*a*) is that a satellite droplet is separated during the droplet retraction stage, which is attributed to the rebound of the substrate. During the period $t^* = 1.0$–1.38, the droplet is retracting; meanwhile, the droplet apex height is increasing. Also, in the second rebound stage of substrate, the momentum transfers from the substrate to the droplet, leading to a greater velocity in the top part of the droplet. When the substrate moves downward again ($t^* = 1.38$–1.89), the velocities of the top and bottom parts of the droplet are opposite and the liquid column continues to deform vertically. Finally, the liquid column begins to neck and eventually separates a satellite droplet ($t^* = 1.89$–2.04).

For the case where $We = 500$ and $K = 0.05$ (see figure 16*c*), corresponding to the MSPR mode, multiple satellite droplets are separated from the mother droplet. The vibration of the substrate is more intense so that an upright liquid ring is formed directly in the region where the medium is gathered ($t^* = 0.43$). This is followed by the merging of the liquid ring into the central liquid column. The velocity difference between different parts of the elongated liquid column leads to the formation of multiple necks and the subsequent generation of multiple separated satellite droplets ($t^* = 1.26$).

For the case where $We = 500$ and $K = 1000$ (see figure 16*d*), corresponding to the SD mode, the droplet exhibits a prompt splashing in the initial stage of impact ($t^* = 0.047$), then experiences a period of oscillations and ultimately deposits on the substrate ($t^* = 1.87$).

5. Conclusions

We have conducted a series of simulations of droplet impact on a flexible circular disk and have focused on the effects of Weber number ($We \in [1, 500]$), substrate stiffness ($K \in [0.01, 1000]$) and contact angle ($\theta = 130°, 60°$) on the droplet–substrate coupling dynamics. According to whether partial droplet separation occurs during impact process, we have distinguished two categories of the impacting modes for the hydrophobic flexible substrate scenario, namely, the intact rebound (IR, e.g. RSR and DSR) and breakup rebound (BR, e.g. JBR, SR or EBR) modes. The effects of the substrate flexibility on the droplet spreading dynamics have been discussed through the time-variation curves of the maximum spreading factor and spreading time, i.e. β_{max} and $T_{\beta_{max}}$. It has been revealed that the substrate rebound will squeeze the fluid at the bottom of the droplet and induces flows from the bottom to the edges, leading to the enhanced spreading of the droplet. Also, when $We \leq 25$ and $K \leq 10$, and the bending stiffness is moderate ($K \sim O(1)$) or lower, the upward movement of the substrate during the late spreading stage will prolongs the spreading time. Further, the spreading process of a droplet on a flexible substrate has been divided into two stages, during which the droplet spreading is suppressed or promoted due to the flexible compliant and rebound mechanisms, respectively; the effect of a flexible substrate on the maximum spreading factor depends on the competition between the two mechanisms. Based on this, a modified scaling law of β_{max} has been proposed by introducing the effective Weber number (We_m). The impact force on a flexible substrate is analysed and we summarise three typical impact force variation processes. We have observed that the extreme values in the deflection curves correspond to the peaks and valleys of the impact force curves. The effect of the droplet on the substrate gradually shifts

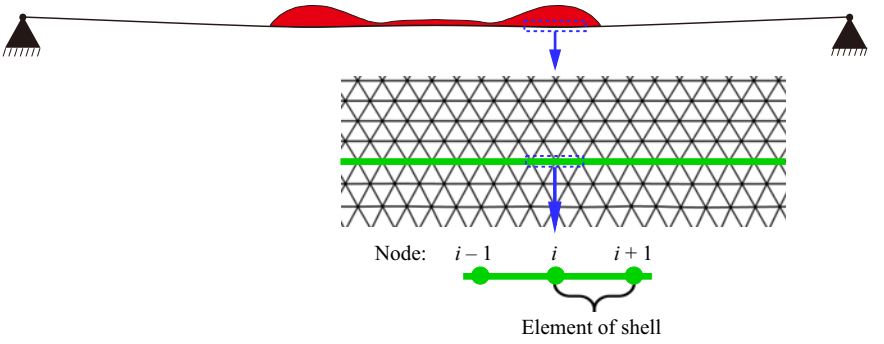

Figure 17. Mesh for shell and fluid domains. The green solid circles and the green solid lines connecting them represent the shell elements, which is located on the midplane of the shell.

from compression to adsorption as the substrate moves upward beyond its initial position. Furthermore, we have performed the analysis of energy and investigated the interaction among droplet kinetic energy, surface energy and total energy of the substrate, and we summarise three typical energy interaction processes, which correspond basically to the three impact force changes, respectively. Finally, the effect of the hydrophilic substrate on the droplet impact dynamics has been examined. Four typical impact modes, i.e. CD, SD, SSPR and MSPR modes, have been classified in the parameter space (K, We) for $\theta = 60°$.

Funding. This research was supported in part by the National Natural Science Foundation of China (nos 12372263, 12372241) and the Natural Science Foundation of Hubei Province of China (no. 2022CFB131).

Declaration of interests. The authors report no conflict of interest.

Author ORCIDs.
Xinping Zhou https://orcid.org/0000-0001-6340-5273;
Qi Zhang https://orcid.org/0009-0007-2552-087X;
Wanqiu Zhang https://orcid.org/0000-0003-0306-9030;
Ze-Rui Peng https://orcid.org/0000-0002-5717-3901.

Appendix A. The mesh for shell and fluid domains

Figure 17 illustrates the local mesh for both shell and fluid domains. The fluid domain is discretised using triangular meshes. To accurately capture the motions of the droplet and the gas around it, the mesh in the region where the droplet moves is refined. In the refined fluid region, the sizes of most triangular elements are approximately equal, and the number and connectivity of elements remain unchanged during the droplet impact process. Moreover, as shown in figure 17, the red solid circles and the blue solid lines connecting them represent the shell elements, which are located on the midplane of the shell. In the simulation, the dynamic mesh deformation is required to account for changes in the geometry of both fluid and shell domains. We can specify mesh refinement criteria and employ adaptive meshing techniques to maintain computational accuracy while capturing complex fluid–structure interactions.

Appendix B. A validation to check the validity of FSI calculations

Figure 18(a) shows the schematic physical model of the fluid–structure interaction benchmark case, which is consistent with Turek & Hron (2006). The key parameters

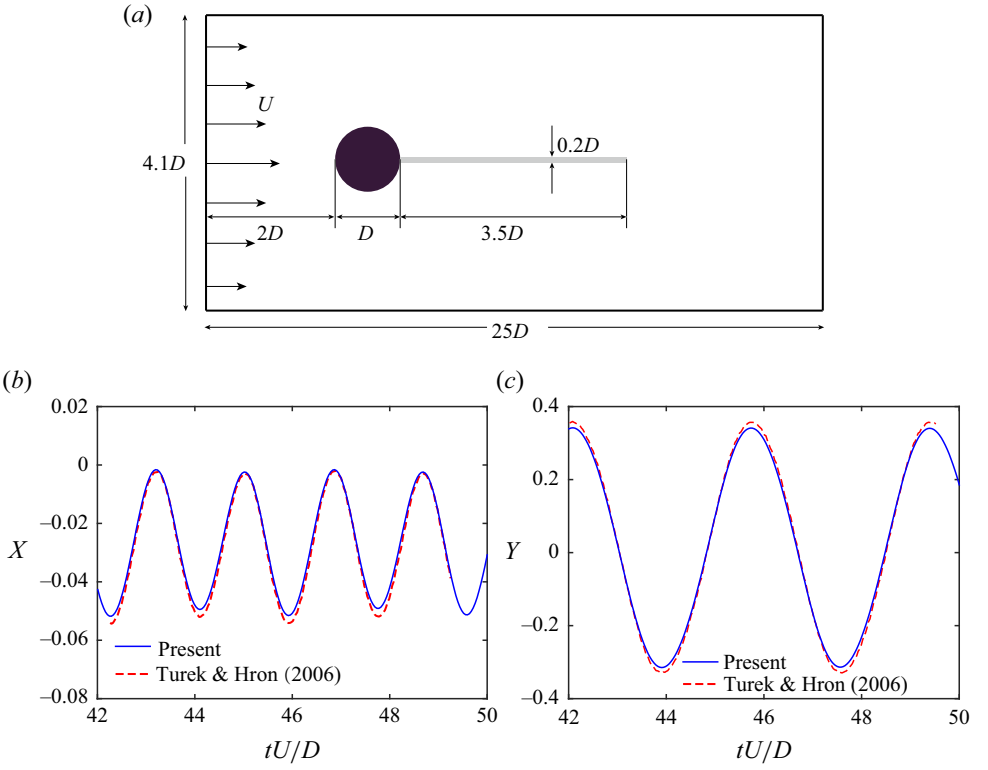

Figure 18. Numerical verification of fluid-structure interaction benchmark case. (*a*) Schematic diagram of a rigid cylinder with a flexible strip in a flow; (*b*,*c*) time variations of (*b*) horizontal and (*c*) vertical positions of strip's trailing edges. The solid and dashed lines represent the results from the present simulations and Turk & Hron (2006), respectively. The key parameters in the simulation are set as follows: fluid density $\rho_l =$ 1000 kg m^{-3}, fluid dynamic viscosity $\mu_l = 1$ Pa ·s, average inflow velocity $U = 2$ m s^{-1}, cylinder diameter $D = 0.1$ m, density of the flexible strip $\rho_s = 1000$ kg m^{-3}, the Young's modulus $E = 5.6$ Mpa and Poisson's ratio $= 0.4$.

in the simulation are set as follows: fluid density $\rho_l = 1000$ kg m^{-3}, dynamic viscosity $\mu_l = 1$ Pa · s, average inflow velocity $U = 2$ m s^{-1}, cylinder diameter $D = 0.1$ m, density of the flexible strip $\rho_s = 1000$ kg m^{-3}, Young's modulus $E = 5.6$ Mpa and Poisson's ratio $= 0.4$. Under these specified values of parameters, the flexible strip will exhibit a flow-induced vibration. Figures 18(*b*) and 18(*c*) shows the time variations of horizontal and vertical positions of strip's trailing edges, respectively. It is evident that the present results are in good agreement with those of Turek & Hron (2006).

References

Abuku, M., Janssen, H., Poesen, J. & Roels, S. 2009 Impact, absorption and evaporation of raindrops on building facades. *Build. Environ.* **44** (1), 113–124.

Bergeron, V., Bonn, D., Martin, J.Y. & Vovelle, L. 2000 Controlling droplet deposition with polymer additives. *Nature* **405**, 772–775.

Chandra, S. & Avedisian, C.T. 1991 On the collision of a droplet with a solid surface. *Proc. R. Soc. Lond.* A **432** (1884), 13–41.

Chen, L., Bonaccurso, E., Deng, P. & Zhang, H. 2016 Droplet impact on soft viscoelastic surfaces. *Phys. Rev.* E **94** (6), 063117.

CLANET, C., BÉGUIN, C., RICHARD, D. & QUÉRÉ, D. 2004 Maximal deformation of an impacting drop. *J. Fluid Mech.* **517**, 199–208.

COLLINGS, E.W., MARKWORTH, A.J., MCCOY, J.K. & SAUNDERS, J.H. 1990 Splat-quench solidification of freely falling liquid-metal drops by impact on a planar substrate. *J. Mater. Sci.* **25**, 3677–3682.

DERBY, B. 2010 Inkjet printing of functional and structural materials: fluid property requirements, feature stability and resolution. *Annu. Rev. Mater. Res.* **40**, 395–414.

DEUFLHARD, P. 1974 A modified Newton method for the solution of ill-conditioned systems of nonlinear equations with application to multiple shooting. *Numer. Math.* **22**, 289–315.

DRESSAIRE, E., SAURET, A., BOULOGNE, F. & STONE, H.A. 2016 Drop impact on a flexible fiber. *Soft Matt.* **12** (1), 200–208.

DU, J.Y., CHAMAKOS, N.T., PAPATHANASIOU, A.G., LI, Y.Z. & MIN, Q. 2021 Jumping velocity of an electrowetting-actuated droplet: a theoretical and numerical study. *Phys. Rev. Fluids* **6** (12), 123603.

EGGERS, J., FONTELOS, M., JOSSERAND, C. & ZALESKI, S. 2010 Drop dynamics after impact on a solid wall: theory and simulations. *Phys. Fluids* **22**, 062101.

GART, S., MATES, J.E., MEGARIDIS, C.M. & JUNG, S. 2015 Droplet impacting a cantilever: a leaf-raindrop system. *Phys. Rev. Appl.* **3** (4), 044019.

GILET, T. & BOUROUIBA, L. 2015 Fluid fragmentation shapes rain-induced foliar disease transmission. *J. R. Soc. Interface* **12** (104), 20141092.

HOWLAND, C.J., ANTKOWIAK, A., CASTREJÓN-PITA, J.R., HOWISON, S.D., OLIVER, J.M., Style, R.W. & Castrejón-Pita, A.A. 2016 It's harder to splash on soft solids. *Phys. Rev. Lett.* **117** (18), 184502.

HUANG, L., SONG, J., WANG, X., ZHAO, C., LIU, Z. & LIU, J. 2018 Soft elastic superhydrophobic cotton: a new material for contact time reduction in droplet bouncing. *Surf. Coat. Technol.* **347**, 420–426.

JOSSERAND, C. & THORODDSEN, S.T. 2016 Drop impact on a solid surface. *Annu. Rev. Fluid Mech.* **48**, 365–391.

JUNG, S., TIWARI, M.K., DOAN, N.V. & POULIKAKOS, D. 2012 Mechanism of supercooled droplet freezing on surfaces. *Nat. Commun.* **3** (1), 615.

KIM, S., WU, Z., ESMAILI, E., DOMBROSKIE, J.J. & JUNG, S. 2020 How a raindrop gets shattered on biological surfaces. *Proc. Natl Acad. Sci. USA* **117** (25), 13901–13907.

LAAN, N., BRUIN, K., BARTOLO, D., JOSSERAND, C. & BONN, D. 2014 Maximum diameter of impacting liquid droplets. *Phys. Rev. Appl.* **2**, 044018.

LEE, J.B., LAAN, N., DE BRUIN, K.G., SKANTZARIS, G., SKANTZARIS, N., DEROME, D., Carmeliet, J. & Bonn, D. 2016 Universal rescaling of drop impact on smooth and rough surfaces. *J. Fluid Mech.* **786**, R4.

LOHSE, D. 2022 Fundamental fluid dynamics challenges in inkjet printing. *Annu. Rev. Fluid Mech.* **54**, 349–382.

MA, Y.F. & HUANG, H.B. 2023 Scaling maximum spreading of droplet impacting on flexible substrates. *J. Fluid Mech.* **958**, A35.

MANGILI, S., ANTONINI, C., MARENGO, M. & AMIRFAZLI, A. 2012 Understanding the drop impact phenomenon on soft PDMS substrates. *Soft Matt.* **8**, 10045–10054.

MISHCHENKO, L., HATTON, B., BAHADUR, V., TAYLOR, J.A., KRUPENKIN, T. & AIZENBERG, J. 2010 Design of ice-free nanostructured surfaces based on repulsion of impacting water droplets. *ACS Nano* **4** (12), 7699–7707.

PEGG, M., PURVIS, R. & KOROBKIN, A. 2018 Droplet impact onto an elastic plate: a new mechanism for splashing. *J. Fluid Mech.* **839**, 561–593.

PEPPER, R.E., COURBIN, L. & STONE, H.A. 2008 Splashing on elastic membranes: the importance of early-time dynamics. *Phys. Fluids* **20** (8), 082103.

RIOBOO, R., TROPEA, C. & MARENGO, M. 2001 Outcomes from a drop impact on solid surfaces. *Atomiz. Sprays* **11**, 155–165.

TUREK, S. & HRON, J. 2006 Proposal for numerical benchmarking of fluid-structure interaction between an elastic object and laminar incompressible flow. In *Fluid-Structure Interaction. Lecture Notes in Computational Science and Engineering* (ed. H.J. Bungartz & M. Schäfer), vol 53, pp. 371–385. Springer.

SIKALO, S., MARENGO, M., TROPEA, C. & GANIC, E.N. 2002 Analysis of impact of droplets on horizontal surfaces. *Exp. Therm. Fluid Sci.* **25** (7), 503–510.

VASILEIOU, T., GERBER, J., PRAUTZSCH, J., SCHUTZIUS, T.M. & POULIKAKOS, D. 2016 Superhydrophobicity enhancement through substrate flexibility. *Proc. Natl Acad. Sci. USA* **113** (47), 13307–13312.

VASILEIOU, T., SCHUTZIUS, T.M. & POULIKAKOS, D. 2017 Imparting icephobicity with substrate flexibility. *Langmuir* **33** (27), 6708–6718.

WEISENSEE, P.B., TIAN, J., MILJKOVIC, N. & KING, W.P. 2016 Water droplet impact on elastic superhydrophobic surfaces. *Sci. Rep.* **6** (1), 30328.

WIRTH, W., STORP, S. & JACOBSEN, W. 1991 Mechanisms controlling leaf retention of agricultural spray solutions. *Pest. Sci.* **33**, 411–420.

XIONG, Y.F., HUANG, H.B. & LU, X.Y. 2020 Numerical study of droplet impact on a flexible substrate. *Phys. Rev.* E **101** (5), 053107.

YEOH, O.H. 1993 Some forms of the strain energy function for rubber. *Rubber. Chem. Technol.* **66**, 754–771.

ZHANG, B., SANJAY, V., SHI, S.L., ZHAO, Y.G., LV, C.J., FENG, X.Q. & LOHSE, D. 2022 Impact forces of water drops falling on superhydrophobic surfaces. *Phys. Rev. Lett.* **129** (10), 104501.